physica status solidi

pss

www.interscience.wiley.com

reprints

WILEY-VCH

REPRINT

Phys. Status Solidi B **246**, No. 1, 183–191 (2009) / **DOI** 10.1002/pssb.200844235

physica status solidi b
www.pss-b.com
basic solid state physics

On the band gap location and core spectra of orthorhombic IV–VI compounds SnS and SnSe

L. Makinistian[*, 1, 2] **and E. A. Albanesi**[**, 1, 2]

[1] INTEC-CONICET, Güemes 3450, 3000 Santa Fe, Argentina
[2] Facultad de Ingeniería, Universidad Nacional de Entre Ríos, 3101 Oro Verde (ER), Argentina

Received 5 June 2008, revised 4 September 2008, accepted 16 September 2008
Published online 22 October 2008

PACS 71.15.Mb, 71.20.Nr, 78.20.Bh, 78.20.Ci

[*] Corresponding author: e-mail lmakinistian@santafe-conicet.gov.ar, Phone: +54 342 455 9174, Fax: +54 342 455 0944
[**] e-mail eaa@santafe-conicet.gov.ar, Phone: +54 342 455 9174, Fax: +54 342 455 0944

While the orthorhombic IV–VI compounds show the typical layered behavior of that crystallography, we show that the presence of sulphur induces important changes to the band gap behaviour: both in its location, and in its character as well. Our modelling of tin sulfide (SnS) and tin selenide (SnSe), performed within an *ab initio* density-functional theory (DFT) with a FP-LAPW method, shows that the spin–orbit interaction produces slight splittings of bands in both compounds, especially in the conduction band, which are in very good agreement with measured values of the core spectra. In addition to these splittings, for SnS we found the novel feature that the spin–orbit relocates the band gap in the BZ, while it does not affect that of SnSe. Furthermore, several aspects of the crystals anisotropy may be explained upon our results on the hybridized band structure, the density of states (DOS) and the optical spectra (complex dielectric function and absorption coefficient). We satisfactorily compare our results with those available in the literature.

1 Introduction The IV–VI compounds' electronic and optical properties make them attractive for their use in diverse technological applications such as cut-off devices and photovoltaic cells, and in the manufacture of infrared lasers [1–3] and detectors. They have also been studied for the evaluation of nanostructures etching [4]. In particular, SnS and SnSe have been used as shells for PbSe and PbS quantum dots, for the development of infrared-based devices [5], and as alternative for Cadmium in IR thin film coatings [6]. Although SnS and SnSe have been experimentally and theoretically assessed [7–16], we present results that to the best of our knowledge were not reported before.

SnS and SnSe crystallize in an orthorhombic structure (Pnma 62 (D_{2h}^{16}) space group) and form double layers that are perpendicular to the direction of the unit cell's largest axis. The unit cell contains 8 atoms organized in two adjacent double layers. The atoms in each double layer bond to their three nearest neighbors and form a chain in zigzag along the direction of the minor axis of the crystal, Fig. 1a–c). The lattice parameters for SnS (SnSe) are $a = 11.200$ Å ($a = 11.4976$ Å), $b = 3.987$ Å ($b = 4.1533$ Å) and $c = 4.334$ Å ($c = 4.440$ Å) [17, 18], corresponding to the $\Gamma \rightarrow X$, $\Gamma \rightarrow Y$ and $\Gamma \rightarrow Z$ directions in the first Brillouin zone (BZ, Fig. 1d), respectively. Because of the dominant Van der Waals character of the bonds between adjacent layers, this material cleaves easily along the b–c [100] planes. All four orthorhombic IV–VI compounds (GeS, GeSe, SnS, SnSe) have an intermediate behavior between a two-dimensional and a three-dimensional material.

In this paper, we present a thorough and updated computational study of SnS and SnSe, based on *ab-initio* calculations of their band structure, density of states (DOS), core spectra, and complex dielectric function and absorption coefficient.

2 Calculation method We have modelled SnS and SnSe using a full potential linearized augmented plane waves (FP-LAPW) method, within the density-functional theory (DFT) [19, 20], as implemented in the WIEN2k package [21].

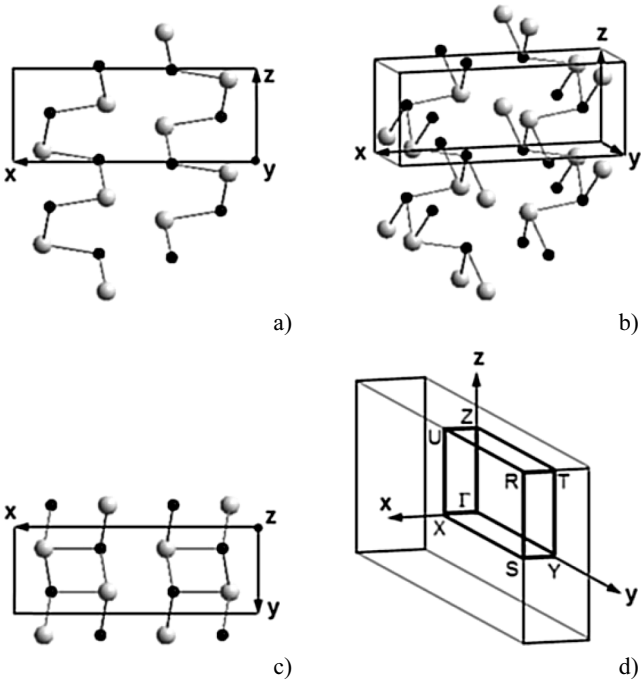

Figure 1 a), b) and c) show different views of the Pnma 62 orthorhombic structure of SnS; d) shows the Brillouin Zone of SnS, with axes *x*, *y* and *z* corresponding to the crystals' axes *a*, *b* and *c*, respectively. The structure (and therefore the BZ) of SnSe is similar to that of SnS.

As part of our approach, we used the local density approximation (LDA) and the Generalized Gradient Approximation (GGA) [22, 23], in the parametrization scheme of Perdew–Burke–Ernzerhof (PBE) [24] for the exchange and correlation potential. This corrected functional is semi-local and thus more sensitive to non-spherical components of the density. Thus, we present all of our results computed with the PBE GGA exchange–correlation potential and with the inclusion of spin–orbit interaction (we also performed the calculations with LDA (with and without spin–orbit), finding that for SnS and SnSe the GGA improvement over LDA is little).

It is to be emphasized, though, that both LDA and GGA always yield underestimated band gaps. An usual correction of this is the scissors operator [25], which can be used even when some non-rigid shifts of bands occur in semiconductors, provided that the *k*-dependence of the error in the excitation energies is negligible. In particular, this approximation is often used in the determination of the band gap offsets [26, 27] in considering interfaces between different semiconductors, and also when optical transitions are studied [28]. Eventhough there are formal theoretical improvements like the GW and BSE methods [29–33], these are still applied in solids using the *k*-independent scissors approximation due to its good performance and also to maintain the volume of calculations in a tractable way [31–33]. Time-dependent DFT (TDDFT) [34] is also making progress in non-linear optical properties such as those showed under the incidence of "strong" laser beams [35] or ultrafast phenomena en semiconductors [36]. In order to perform a detailed analysis of the optical transitions in SnS and SnSe comparing to those of experimentalists, we used a scissors approximation of 0.25 eV; in a similar procedure used previously for the optical spectra of noble metals [37]. Our results for the core spectra discussed in Section 3.3 justify very well our choice.

3 Electronic structure

3.1 Band structure It is to be mentioned that, in both systems (see Figs. 2 and 3), the bands over the $\Gamma \rightarrow X$ line (corresponding to the largest lattice parameter, i.e., to the axis perpendicular to the cleavage plane of the crystal) indicate a strong increase of the charge carriers mobility for the lowest energies of the conduction band, and a strong decrease of the highest of the valence band, in concordance with the strong anisotropy of these systems in that direction.

Also, our calculations allow a comprehensive assessment of hybridization along the different directions of SnS and SnSe (see Figs. 1–3). We notice that the directions involving the Γ-point, are the most hybridized: the spreading and crossing of bands is increased. The $Z \rightarrow U$ and $Y \rightarrow S$ directions are, instead, less symmetrical and hybridization decreases. In Figs. 2b and 3b we plot the band structure in the planes $R \rightarrow U \rightarrow Z \rightarrow T$ and $R \rightarrow S \rightarrow Y \rightarrow T$, showing that only in these special regions the materials become rather decoupled (i.e., less hybridized).

With regards to the energy band gap, our calculations show an interesting situation: both in SnS and SnSe, there seems to be a competition between two possible gaps: G_1 ($C_1 \rightarrow V_1$) on $\Gamma \rightarrow Z$, and G_2 ($C_2 \rightarrow V_2$) on $\Gamma \rightarrow Y$, both of them indirect. See Figs. 2 and 3.

For SnS, the top of the valence band (VBM) occurs at V_1 defining $G_1 = 1.05$ eV. However, V_2 is only 0.03 eV below V_1, and it defines a smaller gap $G_2 = 0.89$ eV. Hence the gap for SnS (G_2) is on $\Gamma \rightarrow Y$, being 0.16 eV lesser than the one on $\Gamma \rightarrow Z$. For SnSe, G_1 and G_2 can also be identified. However, V_2 is 0.13 eV below V_1 being this difference greater than for SnS and rather not neglectable. Therefore, we identify SnSe band gap as being on $\Gamma \rightarrow Z$.

Parke and Srivastava [15] and Car et al. [38] calculated the band structure of SnS and SnSe, respectively using a variation of the pseudopotential method, adjusting their potentials to fit experimental results; and Gashimzade [16] calculated the band structure of SnS and SnSe (and also GeS and GeSe) with a LCAO method. While all these previous calculations show rather decoupled bands, ours show a thorough mixing of bands near E_F, indicating that hybridization is not to be disregarded in these systems. We also tested our calculations without the inclusion of the spin–orbit, as in Ref. [39], finding that this interaction introduces not only changes (splittings) in some regions of the band structure but, for SnS, does it also qualitatively redefine the location of the band gap in the BZ. Indeed,

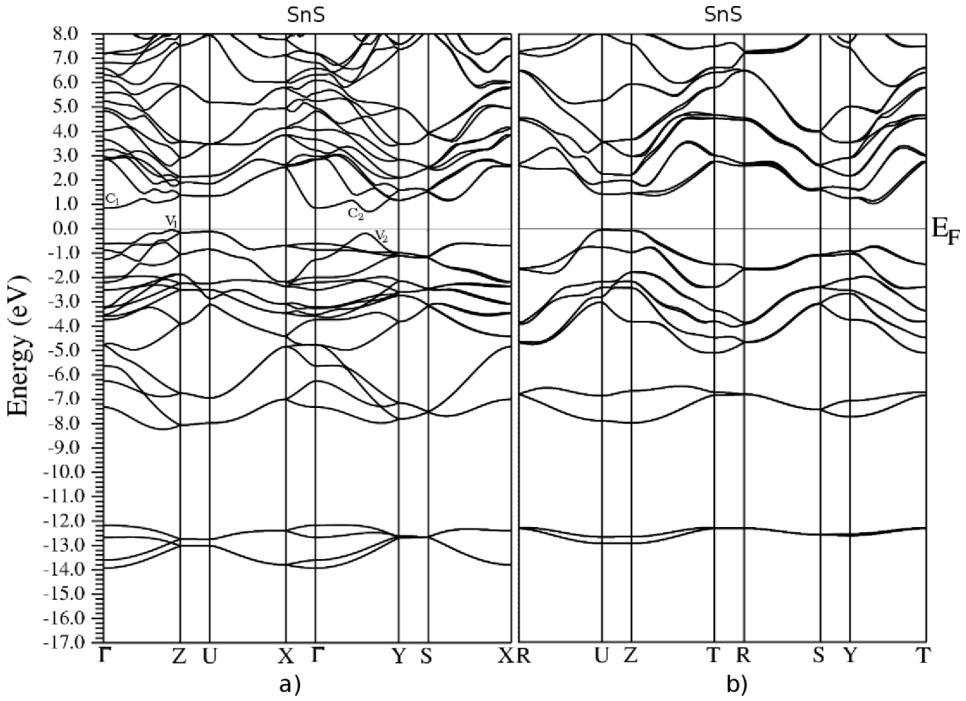

Figure 2 Band structure of SnS with spin–orbit interaction a) in a most symmetrical path and b) in a less symmetrical path in the BZ.

were it not for the spin–orbit interaction, the SnS band gap would be in $\Gamma \rightarrow Z$ (as for SnSe) instead of in $\Gamma \rightarrow Y$, as we show in this work, to the best of our knowledge for the first time.

3.2 Densities of states (DOS) In order to facilitate the following discussions, we are presenting the composition of the peaks V_1 through V_8 in the valence bands and of $A-B$, $A'-B'$, $b-b'$ and C_1 through C_5 of the conduction band of the DOS as they are shown in Fig. 4 (bottom floor), in terms of states type, and the kind of atom from which they are originated, see Table 1.

The total and partial (s, p and d atomic orbitals) densities of states obtained in this work are shown in Fig. 4. In this figure, our total DOS is compared to experimental curves obtained with photoemission measurements [9, 10,

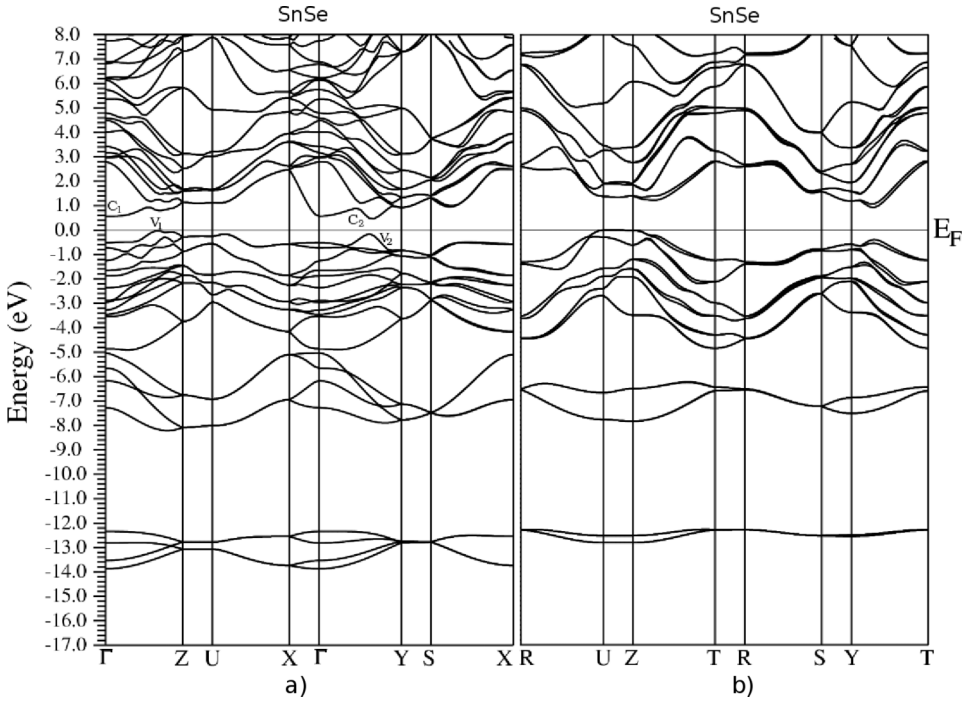

Figure 3 Band structure of SnSe with spin–orbit interaction a) in a most symmetrical path and b) in a less symmetrical path in the BZ.

Table 1 Relevant calculated DOS peaks (in eV) and their contributing states. Note that whenever the contributions of p_x, p_y and p_z orbitals are equal, we simply put "p-", otherwise we present the orbitals in decreasing order of contribution. When contributions for SnS and SnSe are different the latter's are consigned between parenthesis.

DOS peak	DOS energy		contributing states	
	SnS	SnSe	main	minor
V_8	−7.23	−7.27	s-Sn	p-anion
V_7	−6.59	−6.59	s-Sn	p-anion
V_6	−4.40	−4.28	p-anion	p-Sn
V_5	−3.48	−3.40	$p_{z(x)}$, $p_{x(z)}$, p_y-S (Se)	p_z, p_x, p_y-Sn
V_4	−2.64	−2.60	p-anion	p-Sn
V_3	−2.08	−1.88	p_y, $p_{x(z)}$, $p_{z(x)}$-S (Se)	p-Sn
V_2	−1.16	−1.20	$p_{x(y)}$, $p_{y(x)}$, p_z-S (Se)	p_y, p_x, p_z-Sn, s-Sn
V_1	−0.53	−0.65	p_y, p_x, p_z-anion	p_y, p_x, p_z-Sn, s-Sn
VBM	0	0	p_x-anion, s-Sn	p_y, p_z-anion
$A-B$	1.95	1.50	$p_{y(z)}$, $p_{z(x)}$, $p_{x(y)}$-Sn	s-Sn, p-anion, s-anion
$A'-B'$	2.20	1.79	p_x, p_z-Sn	p_y-Sn, s-Sn, p-anion, s-anion
$b-b'$		2.37	p_x, p_z, p_y-Sn	p-Se
C_1	2.77	3.27	p_x,(p_y), p_z-Sn	p_y-Sn, p_x, p_z, p_y-anion
C_2	3.44	3.84	p_x-Sn	$p_{y(z)}$, $p_{z(y)}$-Sn, p_x, p_z, p_y-anion
C_3	4.26	4.71	p_x-Sn	p_y, p_z-Sn, p_x, p_z, p_y-anion
C_4	4.81	5.21	$p_{y(z)}$, $p_{z(y)}$-Sn	p_x-Sn, p-anion
C_5	5.48		p_y-Sn	p_z, p_x-Sn, p_y, p_z, p_x-S

13] and to theoretical DOS calculations performed with the LCAO method [16]. In particular for SnS, our calculations predict a fine structure of the top valence band coinciding with the three experimental measurements (see peaks at −0.88 eV, −2.32 eV and −6.38 eV (and also −12.54, for Kemeny's [10] curve), and the deep valley, at −1.68 eV).

The resemblance between theory and experiment for SnSe is almost as good as for SnS, except for Shalvoy's DOS lacking the valley arround –1.44 eV, which the other two experimental results do show. We believe this is most likely due to the fact that Shalvoy et al. [9] worked with polycrystalline samples, unlike the other experimentalists, who used monocrystals.

The DOS calculated with the LCAO method is in an acceptable accordance as to the lower part of the conduction band, the order of magnitude of the band gap, and the overall presentation of three clearly different regions of the valence band. However, due to their implementation with interactions only to nearest neighbors, this calculations clearly fail to account for the remarkable hybridization shown at the upper part of the valence band, exaggerating the layered feature of the material.

Also, our results make a prediction that to our knowledge had not been reported so far, i.e., the presence of an important contribution of s-cation states to the top of the valence band (see Fig. 4, first floors). We assign the presence of these s-cation states, hybridized with the p-cation and p-anion contributions, as the most important feature in defining most physical properties (since they shape the behavior of the maximum that determines the band gap). This had already been found to be the key in the band gap formation of the cubic IV−VI compounds [26, 40]. It is also well established the resemblance between the physical properties of orthorhombic IV−VI materials among themselves [9, 13]. Therefore, based on the afore said, in spite of being aware of the differences between cubic and orthorhombic IV−VI compounds, we suggest this behavior of the s-cation states at the edge of the valence band to be the fingerprint of the IV−VI compounds, that any description should achieve in order to accurately describe this family of compounds.

3.3 Core spectra By measuring the partial-yield spectra of $SnS_{0.9}Se_{0.1}$ and SnSe, Taniguchi et al. [13] studied the absorption spectrum in the core excitation region, for the electric field parallel to c (called a in their paper) and b axes, $E\|c$ and $E\|b$, respectively. They associated it with the interaction of the 4d-Sn core levels (cation spectra) and the 2p-S ($SnS_{0.9}Se_{0.1}$) and 3p-Se (SnSe) core levels (anion spectra) with the conduction bands.

With reference to the cation spectra, both for $SnS_{0.9}Se_{0.1}$ and SnSe, we can explain the $A-B$ and $A'-B'$ structures of Taniguchi et al. [13] as originated from a cooperative effect produced by relatively flat bands in different regions of the BZ (see Figs. 1–4), together with the rest of the mixed bands about each energy in the whole BZ. For SnS, our first peak is at 1.95 eV, 0.81 eV above the conduction band minimum (CBM) (1.50 eV, 0.65 eV above the CBM, for SnSe), while our second peak is, also well defined, at 2.20 eV, 1.06 eV above CBM (1.79 eV, 0.94 eV above the CBM, for SnSe). These give our theoretical fine structure $A-B$ and $A'-B'$ splitting of 0.35 eV (0.29 eV for SnSe), to be compared with the 0.22 eV (0.32 eV for SnSe) $A-B$ experimental value for $E\|c$, and 0.25 eV (0.26 for SnSe) for $E\|b$ measurements ($A'-B'$ is not available, since B′ was not observed), see Table 2. Therefore, we show how our results on the conduction bands are qualitatively and quantitatively compatible with Taniguchi et al. [13] measurements.

Table 2 Our theoretical core spectra, compared to Taniguchi et al. [13] experimental cation and anion spectra results. All values in eV.

		ours	expt. [13]	
			for $E\|c$	for $E\|b$
cation spectra	$SnS_{0.9}Se_{0.1}$, our SnS	0.35	0.22	0.25
	SnSe	0.29	0.32	0.26
anion spectra	$SnS_{0.9}Se_{0.1}$, our SnS	0.65	0.7	0.7
	SnSe	2.37	2.30	2.30

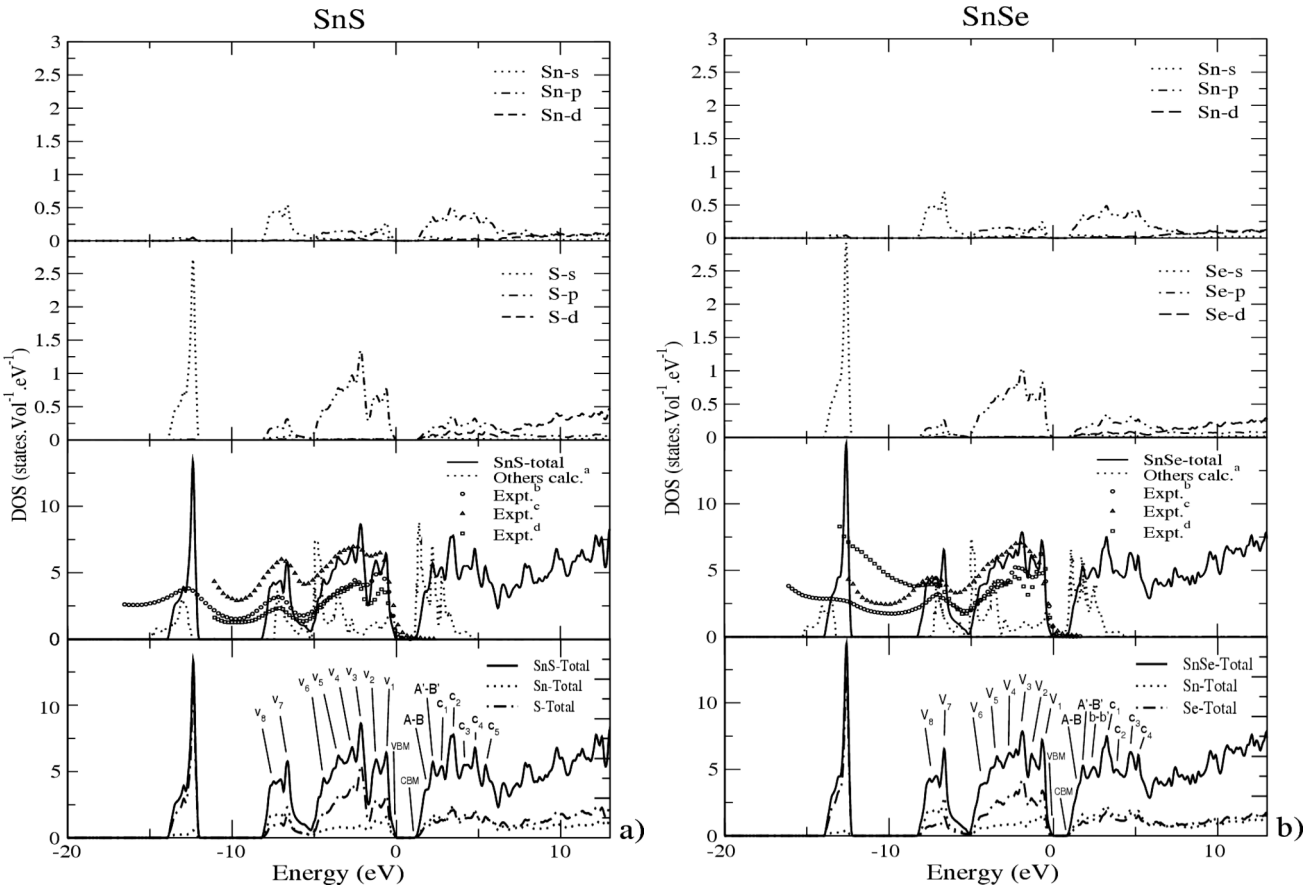

Figure 4 Atom discriminated DOS of s-, p- and d-orbitals of SnS and SnSe. Total density: our calculation, other's calculation [a] Ref. [25], and experimental results, [b] Ref. [14], [c] Ref. [13], and [d] Ref. [17]. For clarity, in the bottom plot we repeat our total DOS and label important peaks.

Taniguchi et al. [13] also measured the anion partial-yield spectra of $SnS_{0.9}Se_{0.1}$ and SnSe, for $E\|c$ and $E\|b$ (see Table 2). For $SnS_{0.9}Se_{0.1}$, they measured two broad structures, called a and a', at 162.5 eV and 163.8 eV both for $E\|c$ and $E\|b$. Therefore they assign the experimental structure a–a' as the transition to the first peak 0.7 eV above the CBM, in excellent agreement with our corresponding value A–B of 0.65 eV above the CBM.

For the anion spectra of SnSe, they measured three broad structures, called a, a' and b, at 54.7 eV, 55.6 eV and 56.2 eV, respectively, both for $E\|c$ and $E\|b$. An expected partner of b, b', was not resolved by the experiments. Given that the 3d-Se core level splitting is of 0.85 eV, they assign their structure a–a' (0.90 eV) to it. In our calculation b–b' (see Fig. 4) is at 2.37 eV, which is in excellent agreement with the experimental value (2.30 eV) of Ref. [13].

4 Optical properties

4.1 Calculation details Out of our electronic structure calculations, we determine the imaginary part of the complex dielectric function $\varepsilon_2(\omega)$ integrating in k-space (by the standard tetrahedron-method [41]). The expression for the complex dielectric tensor in the LDA (GGA) scheme is [42]:

$$\varepsilon_2(\omega)_{\alpha\beta} = \frac{4\pi^2 e^2}{m^2\omega^2}\sum_{i,f}\int\langle f|\, p_\alpha|i\rangle\langle i|\, p_\beta|f\rangle\, W_i(1-W_f) \times \delta(E_f - E_i - \hbar\omega)\,\mathrm{d}^3k\,, \quad (1)$$

where, $\langle f|p_\alpha|\, i\rangle$ and $\langle i|p_\beta|f\rangle$ are the dipole matrix elements corresponding to the α and β directions of the crystal (x, y or z), and f, i, are the final and initial states, respectively, W_n is the Fermi distribution function for the n-th state, and E_n is the electron energy of the n-th state. The real part of the diagonal dielectric functions is computed using the Kramers–Kronig relations in the form

$$\varepsilon_1(\omega)_{\alpha\alpha} = 1 + \frac{2}{\pi}P\int_0^\infty \frac{\omega'\varepsilon_2(\omega')_{\alpha\alpha}}{\omega'^2-\omega^2}\,\mathrm{d}\omega'\,, \quad (2)$$

where P means the principal value of the integral. In order to achieve a comprehensive understanding of the optical behavior of the system, having computed the complex dielectric function, we then calculated the coefficient of

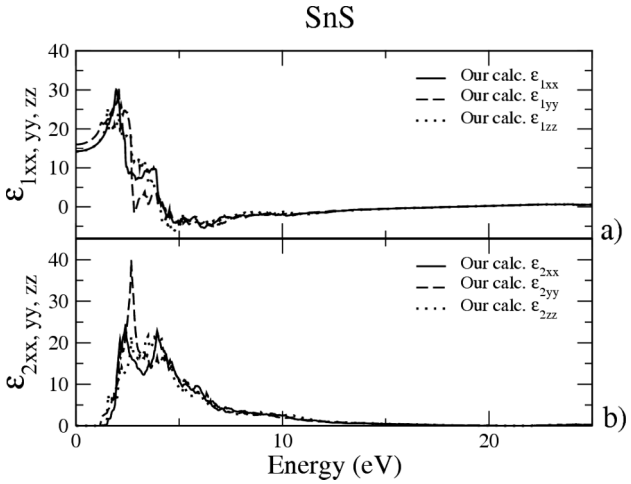

Figure 5 Our calculated dielectric function (real and imaginary parts) for SnS.

absorption $\alpha(\omega)$ as

$$\alpha(\omega)_{\alpha\alpha} = \frac{2\omega}{c}\left(\frac{|\varepsilon(\omega)_{\alpha\alpha}| - \varepsilon_1(\omega)_{\alpha\alpha}}{2}\right)^{1/2} \quad (3)$$

and the reflectivity $R(\omega)$ as

$$R(\omega)_{\alpha\alpha} = \frac{1-\sqrt{2}\left(|\varepsilon(\omega)_{\alpha\alpha}| + \varepsilon_1(\omega)_{\alpha\alpha}\right)^{1/2} + |\varepsilon(\omega)_{\alpha\alpha}|}{1+\sqrt{2}\left(|\varepsilon(\omega)_{\alpha\alpha}| + \varepsilon_1(\omega)_{\alpha\alpha}\right)^{1/2} + |\varepsilon(\omega)_{\alpha\alpha}|}, \quad (4)$$

where $|\varepsilon(\omega)_{\alpha\alpha}| = (\varepsilon_1^2(\omega)_{\alpha\alpha} + \varepsilon_2^2(\omega)_{\alpha\alpha})^{1/2}$.

As to convergence, we found that a 108 k-points calculation did not converge, while 1440 and 2142 k-points calculations coincided almost exactly. Therefore, we assumed convergence at 2142 and calculated the optical parameters with this sampling of the irreducible part of the BZ.

Finally, we realize that electronic excitations such as those involved in optical absorption and dispersion should formally be described within a theory involving time, so that the dependence of the system's eigenvalues on the time variation of the incident field (light) is taken into account. For example, Bruneval et al. [43] focus on the importance of screening the long range components of the exchange interaction in three theoretical approaches: TD-DFT within the "exact exchange" approximation (TD-EXX), Many Body Perturbation Theory (MBPT) and a method refered to as ρ/G, which combines the MBPT with the density functional concept. They demonstrate that the mentioned screening improves the results for absorption spectra of bulk silicon, and so presumably of semiconductors in general. Also, Botti et al. [44] showed that for solids exhibiting a strong continuum excitonic effect a long range contribution to the exchange–correlation kernel of a TDDFT substantially improves the calculation. They discuss the range of applicability of this contribution, and its use for the prediction of continuum excitonic effects. Working on the same line, Sottile et al. [45] analize in detail the behaviour of the optical absorption and the electron energy loss in finite and infinite systems. In this work, we obtain calculated optical spectra within the simplified scheme described above, finding that in the particular case of SnS and SnSe, the sole application of a rigid scissors operator already performs a fine approximation. This suggest that effects beyond DFT play at most a minor role in determining the optical functions of these systems in the studied region.

4.2 General features A general difference between SnS and SnSe is that optical spectra of the latter are, in general, greater than the ones for SnS. For example, the maxima of ε_{2xx}, ε_{2yy} and ε_{2zz} for SnSe are about ~8%, ~27%, and ~56% greater than the corresponding ones in SnS. This feature implies a stronger effect of SnSe on the incoming radiation (both regarding dispersion and absorption). Thus we propose it could be taken into account as an efficiency determining factor, were this materials be evaluated for the implementation of electro-optical devices.

As to the directional behavior of the materials under study, an overall 3D anisotropic behavior is observed, which could be taken advantage of in the design of sensors with multidirectional functionality.

4.3 Dispersion $\varepsilon_1(\omega)$ For SnS (Fig. 5), in the direction of axis a, $\varepsilon_{1xx}(\omega)$ presents a sharp peak followed by a relatively deep valley and then another less intense, more blunt peak. There are also shoulders and minor peaks in the abnormal dispersion region and on the rising terminal tail of this function. SnSe (Fig. 6) presents a similar morphology except for, although also presenting a sharp peak, it shows a rough shoulder instead of the valley and peaks observed in SnS.

Both for SnS and SnSe, along the minor axis b (yy), a broad peak with a complex fine structure is observed for $\varepsilon_{1yy}(\omega)$. This structure is followed by a steep falling edge, almost vertical in the case of $\varepsilon_{1yy}(\omega)$, and then several minor peaks and shoulders. As regards $\varepsilon_{1zz\text{-SnS–SnSe}}$, the steep falling edge is substituted by a slow convex fall, accidented with a fine structure of minor peaks and shoulders.

4.4 Absorption $\varepsilon_2(\omega)$, $\alpha(\omega)$ For SnS (Fig. 5 and Table 3) in the direction of axis a, $\varepsilon_{2xx}(\omega)$ presents two sharp peaks, E_1 and E_2 with a relatively deep valley in between. SnSe (Fig. 6 and Table 3) also presents this features, only with the valley being less deep, and the second peak, E_2, being less sharp and followed by a plateau, E_3 (extended from ~3.5 eV to ~4.10 eV). In the yy direction a very acute peak, E_2, is seen in both systems, followed by a clearly defined shoulder in SnS (E_3), which is not present in $\varepsilon_{2yy\text{-SnSe}}$. Lastly, ε_{2zz} shows a lower and broader general aspect without remarkably distinct features for SnS and SnSe. All three spectra (i.e. for each of the three axes) are completed toward greater energies with a descending tail accidented with minor, though clearly discernible peaks and shoulders (E_{4-7}). Tables 1 and 3

Table 3 Imaginary part of the complex dielectric function of SnS and SnSe. Energies are in eV.

SnS									SnSe								
DOS	ε_{2xx}		ε_{2yy}			ε_{2zz}			DOS	ε_{2xx}		ε_{2yy}			ε_{2zz}		
	peak	our calc.	peak	our calc.	expt.	peak	our calc.	expt.		peak	our calc.	peak	our calc.	expt.	peak	our calc.	expt.
	E_0	1.54	E_0	1.21	1.21[a]	E_0	1.54	1.54[a]		E_0	1.09	E_0	0.93	1.38[a]	E_0	1.14	1.44[a]
						E_1	1.6		$V_{VBM} \rightarrow A'-B'$			E_1	1.81		E_1	1.81	
						E_2	2.23		$V_1 \rightarrow A-B$	E_1	2.09	E_2	2.14	2.20[a]			
$V_1 \rightarrow A-B$	E_1	2.44							$V_1 \rightarrow A'-B'$			E_3	2.38	2.35[a]	E_2	2.41	2.53[a]
$V_{VBM} \rightarrow C_1$			E_1	2.72	2.81[a]	E_3	2.72	3.08[a]	$V_2 \rightarrow A-B$			E_4	2.81		E_3	2.81	3.01[a]
$V_{VBM} \rightarrow C_2$			E_2	3.41		E_4	3.47		$V_3 \rightarrow A-B$	E_2	3.24						
$V_1 \rightarrow C_2$	E_2	3.99	E_3	4.17	4.17[a]	E_5	3.93	3.90[a]	$V_3 \rightarrow b-b'$	E_3	3.78	E_5	3.53	3.96[a]	E_4	3.50	3.87[a]
$V_2 \rightarrow C_2$	E_3	4.59							$V_2 \rightarrow C_1$	E_4	4.66	E_6	4.50		E_5	4.29	
$V_2 \rightarrow C_3$	E_4	5.32	E_4	5.29					$V_3 \rightarrow C_2$	E_5	5.69				E_6	5.74	
$V_4 \rightarrow C_2$	E_5	5.92				E_6	6.01		$V_4 \rightarrow C_2$			E_7	6.16	6.32[a]			
$V_3 \rightarrow C_3$			E_5	6.34					$V_3 \rightarrow C_4$	E_6	7.02						
$V_6 \rightarrow C_1$	E_6	7.34							$V_7 \rightarrow A'-B'$			E_8	8.46	9.37[a]	E_7	8.34	9.16
$V_5 \rightarrow C_4$						E_7	8.40	8.40[a]	$V_8 \rightarrow A-B$	E_7	8.83						
$V_7 \rightarrow C_1$			E_6	9.13	10.22[a]				$V_7 \rightarrow C_1$	E_8	9.83						
$V_8 \rightarrow b-b'$	E_7	9.98															

[a] Ref. [12]

permit to track the origin of all peaks. For example, peaks $\varepsilon_{2yy\text{-E3}}$ and $\varepsilon_{2zz\text{-E3}}$ (both at 2.72 eV) of SnS are assigned to a transition $V_{VBM} \rightarrow C_1$, mainly from p_x-S and s-Sn orbitals in the valence band to p_x, p_z-Sn orbitals in the conduction band. For ε_2 the higher anisotropy occurs in the range ~2.00–4.50 eV for SnS, and of ~1.70–3.90 eV for SnSe.

As to the coefficient of absorption, details can be appreciated in the insets of Fig. 7. An isotropic gap of 1.16 eV is observed for SnS, while $\alpha_{xx\text{-E0}}$ and $\alpha_{zz\text{-E0}}$ happen at 0.88 eV and $\alpha_{yy\text{-E0}}$ at 0.85 eV in SnSe. However, they become clearly anisotropic as the absorption edges rise, also presenting strong anisotropy in the ranges ~2.10–3.90 eV and ~2.00–3.30 eV, for SnS (E_{1-3}) and SnSe (E_{1-5}), respectively. In SnS, α_{xx} and α_{zz} show an abrupt change of slope at arround 1.5 eV, while this sudden change is not observed for the *yy* direction, which shows a smooth shoulder (E_1) instead.

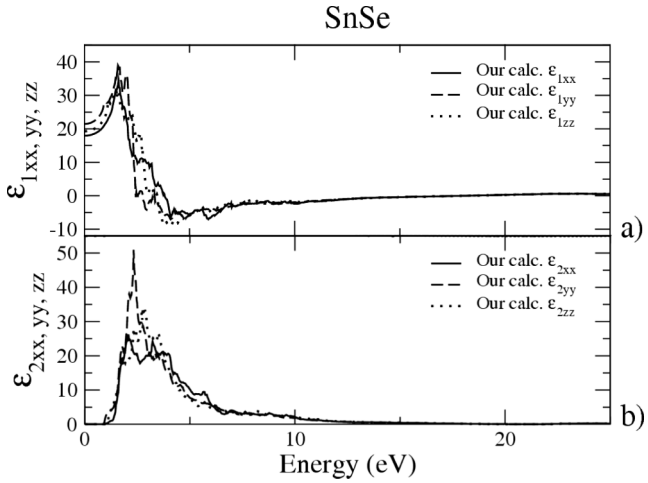

Figure 6 Our calculated dielectric function (real and imaginary parts) for SnS.

With regards to reflectivities at zero energy, they are, for *xx*, *yy* and *zz* axes of 0.33, 0.36 and 0.34 (SnS) and 0.37, 0.41 and 0.39 (SnSe). They all rise and keep fluctuating around the value of 0.5 (i.e. 50%), only to abruptly drop at about 18.00 eV. Except for a rather isotropic region, ~13.50–16.10 eV and ~13.80–16.70 eV for SnS and SnSe, respectively, the three axes present a clearly anisotropic behavior.

4.5 Interaction between the double layers As discussed for GeS by Grandke and Ley [46], besides spin–orbit, the interaction between the double layers also produces splitting of bands. According to our calculations, this latter effect is stronger than the one due to spin–orbit. The effect can be seen most clearly for the two deepest bundle of bands discussed in Section 3.1. As to the region of higher energies and up to E_F, the strong hybridization of bands prevents the effect from becoming evident. The double layer interaction shows itself relevant in the least symmetrical regions, in the $R \rightarrow U$, $Z \rightarrow T$ and $Y \rightarrow T$ directions of the BZ, occurring mainly for the 5s-Sn levels (see Figs. 2 and 3). The splitting of these flat bands originates the peaks v_7 and v_8 in Fig. 4.

5 Conclusions We used, within DFT, an *ab initio* FP-LAPW method to show the proper location of the band gap of the semiconductors SnS and SnSe. The location is produced by the spin–orbit effect, which affects specially the conduction band. Our model is in very good agreement with measured values of the core spectra. We also studied the optical properties of these compounds, showing that the LDA approximation yields results very similar to those of

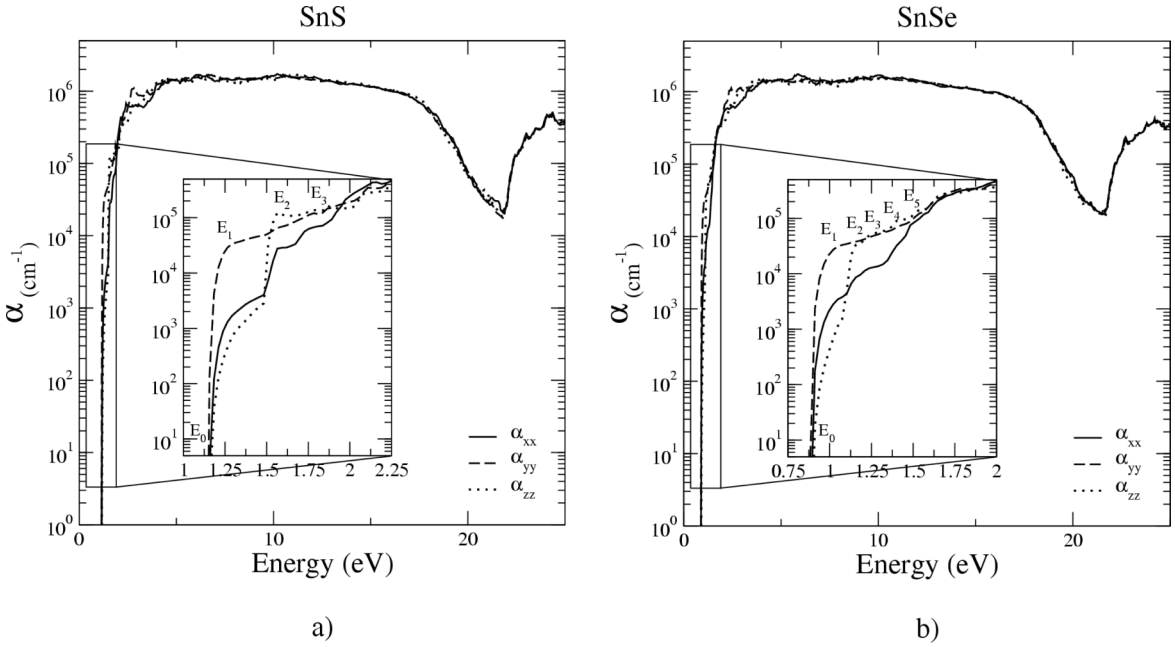

Figure 7 Our calculated coefficient of absorption for both SnS and SnSe.

GGA, and in coincidence with the experimental values. We pose the behavior of the cationic s-states as characteristic of the IV–VI materials, also proving that any theoretical description of these material needs to account for the s–p hybridization of the valence band in order to give a proper description of the band structure. Finally, we showed the non-neglectable hybridizing effect of the double layer interaction.

Acknowledgements The authors acknowledge financial support from the Consejo Nacional de Investigaciones Científicas y Técnicas (CONICET), the Universidad Nacional de Entre Ríos (UNER), and the Agencia Nacional de Promoción Científica y Tecnológica (ANPCyT), Argentina.

References

[1] Z. Shi, G. Xu, P. J. McCann, X. M. Fang, N. Dai, C. L. Felix, W. W. Bewley, I. Vurgaftman, and J. R. Meyer, Appl. Phys. Lett. **6**(25), 3688 (2000).
[2] T. Schwarzl, M. Böberl, W. Heiss, G. Springholz, J. Fürst, and H. Pascher, Proc. GMe Forum 103 (2003).
[3] M. Böberl, W. Heiss, T. Schwarzl, K. Wiesauer, and G. Springholz, Appl. Phys. Lett. **82**(23), 4065 (2003).
[4] Th. Schwarzl, W. Hei, G. Kocher-Oberlehner, and G. Springholz, Semicond. Sci. Technol. **14**, L11 (1999).
[5] J. Shan, F. C. J. M. van Veggel, M. Raudsepp, A. G. Pattantyus-Abraham, and J. F. Young, Technical Proceedings of the 2006 NSTI Nanotechnology Conference and Tradeshow, Vol. 3.
[6] S. J. Wakeham, G. J. Hawkins, G. R. Henderson, and N. A. Carthey, Proc. SPIE, Optics and Photonics Conference, Advances in Thin-Film Coatings for Optical Applications III (2006).
[7] T. H. Patel, R. Vaidya, and S. G. Patel, Bull. Mater. Sci. **26**(6), 569 (2003).
[8] A. Agarwal, P. H. Trivedi, and D. Lakshmiranayana, Cryst. Res. Technol. **40**(8), 789 (2005).
[9] R. B. Shalvoy, G. B. Fisher, and P. J. Stiles, Phys. Rev. B **15**, 2021 (1977).
[10] P. C. Kemeny, J. Azoulay, M. Cardona, and L. Ley, Nuovo Cimento B **39**(2), 709 (1977).
[11] Li-Ming Yu, A. Degiovanni, P. A. Thiry, J. Ghijsen, and R. Caudano, Phys. Rev. B **47**, 16222 (1993).
[12] R. Eymard, and A. Otto, Phys. Rev. B **16**, 1616 (1977).
[13] M. Taniguchi, R. L. Johnson, J. Ghijsen, and M. Cardona, Phys. Rev. **42**(6), 3634 (1990), and references therein.
[14] A. Tanuevski, Semicond. Sci. Technol. **18**, 501 (2003).
[15] A. W. Parke and G. P. Srivastava, phys. stat. sol. (b) **101**, K31 (1980).
[16] F. M. Gashimzade, D. G. Guliev, D. A. Guseinova, and V. Y. Shteinshrayber, J. Phys.: Condens. Matter **4**, 1081 (1992).
[17] L. Ehm, K. Knorr, P. Dera, A. Krimmel, P. Bouvier, and M. Mezouar, J. Phys.: Condens. Matter **16**, 3545 (2004).
[18] D. Pathinettam Padiyan and A. Marikani, Cryst. Res. Technol. **37**(11), 1241 (2002).
[19] L. H. Thomas, Proc. Camb. Philos. Soc. **23**, 542(1927).
E. Fermi, Z. Phys. **48**, 73(1928).
P. Hohenberg and W. Kohn, Phys. Rev. **136**, 864B (1964).
[20] W. Kohn and L. J. Sham, Phys. Rev. **140**, 1133A (1965).
[21] P. Blaha, K. Schwarz, and J. Luitz, Vienna University of Technology (2001).
Improved and updated version of the WIEN code, published by P. Blaha, K. Schwarz, P. Sorantin, and S. B. Rickey, Comput. Phys. Commun. **59**, 399 (1990).
[22] J. P. Perdew, J. A. Chevary, S. H. Vosko, K. A. Jackson, M. R. Pederson, D. J. Sing, and C. Fiolhais, Phys. Rev. B **46**, 6671 (1992).
[23] J. P. Perdew and Y. Wang, Phys. Rev. B **45**, 13244 (1992).

[24] J. P. Perdew, K. Burke, and M. Ernzerhof, Phys. Rev. Lett. **77**, 3865 (1996); Phys. Rev. Lett. **78**, 1396 (1997).
J. P. Perdew, S. Kurth, A. Zupan, and P. Blaha, Phys. Rev. B **82**, 2544 (1999).
[25] R. Del Sole and R. Girlanda, Phys. Rev. B **48**, 11789 (1993).
[26] S. Wey, A. Zunger, Phys. Rev. B **55**, 13605 (1977).
[27] E. A. Albanesi, W. L. Lambrecht, and B. Segall, J. Vac. Sci. Technol. B **12**, 2470 (1994).
[28] R. Laskowski, N. E. Christensen, G. Santi, and C. Ambrosch-Draxl, Phys. Rev. B **72**, 035204 (2005).
[29] Z. H. Levine, D. C. Allan, Phys. Rev. Lett. **63**, 16 (1989).
[30] G. Onida, L. Reining, and A. Rubio, Rev. Mod. Phys. **74**, 601 (2002).
[31] A. Arnaud and M. A. Allouani, Phys. Rev. B **63**, 085208 (2001).
B. Arnaud and M. Alouani, Phys. Rev. B **62**, 4464 (2000).
[32] Christensen, K. Hummer, and C. Ambrox-Draxl, Phys. Rev. B **71**, 081202-1 (2005).
[33] F. Ladstädter, U. Hohenester, P. Pusching, and C. Ambrosch-Draxl, Phys. Rev. B **70**, 235125-1 (2004).
[34] K. Burke, J. Wershcnik, and E. K. U. Gross, J. Chem. Phys. **123**, 062206 (2005).
[35] M. A. L. Marques and E. K. U. Gross, Annu. Rev. Phys. Chem. **55**, 427 (2004).
[36] V. Turkowski and C. A. Ullrich, Phys. Rev. B **77**, 075204 (2008).
[37] K. Stahrenberg, Th. Herrmann, K. Wilmers, N. Esser, W. Richter, and M. J. G. Lee, Phys. Rev. B **64**, 115111 (2001).
[38] R. Car, G. Ciucci, and L. Quartapelle, phys. stat. sol. (b) **86**, 471 (1978).
[39] Z. Nabi, A. Kellou, S. Mécabih, A. Khalfi, and N. Benosman, Mater. Sci. Eng. B **98**, 104 (2003).
[40] E. A. Albanesi, E. C. Okoye, C. O. Rodriguez, E. L. Peltzer y Blanca, and A. G. Petukhov, Phys. Rev. B **61**, 16589 (2000).
[41] P. E. Bröchl, O. Jepsen, and O. K. Andersen, Phys. Rev. B **49**, 16223 (1994).
[42] C. Ambrosch-Draxl, R. Abt, authors of the code extension for optical properties, The calculation of optical properties within WIEN97, ICTP Lecture Notes (1998), unpublished.
[43] F. Bruneval, F. Sottile, V. Olevano, and L. Reinig, J. Chem. Phys. **124**, 144113 (2006).
[44] S. Botti, F. Sottile, N. Vast, V. Olevano, L. Reining, H. Weissker, A. Rubio, G. Onida, R. Del Sole, and R. W. Godby, Phys. Rev. B **69**, 155112 (2004).
[45] F. Sottile, F. Bruneval, A. G. Marinopolulos, L. K. Dash, S. Botti, V. Olevano, N. Vast, A. Rubio, and L. Reining, Int. J. Quantum Chem. **102**, 684 (2005).
[46] T. Grandke and L. Ley, Phys. Rev. B **16**, 832 (1977).